



# Manganese doping regulated the built-in electric field of FeBTC for enhanced photoelectrocatalytic hydrolysis

Yi-Wen Dong, Hai-Jun Liu, Xiao Wang, Fu-Li Wang, Xin-Yu Zhang, Qian-Xi Lv, Chun-Ying Liu, Yong-Ming Chai\*, Bin Dong\*

State Key Laboratory of Heavy Oil Processing, College of Chemistry and Chemical Engineering, China University of Petroleum (East China), Qingdao 266580, PR China

## ARTICLE INFO

### Keywords:

Oxygen evolution reaction  
Mott Schottky heterojunction  
Built-in electric field  
Light absorption capacity  
Photo-electrocatalytic

## ABSTRACT

MOF-based Mott Schottky heterojunction has been researched as a promising photoelectrocatalytic material for oxygen evolution reaction (OER), but activity is severely limited by built-in electric field (BIEF). In this study, trace Mn doping strategy is used to enhance the BIEF of FeBTC/NiF, and the energy level configuration is also adjusted. Prepared Mn-FeBTC/NiF has excellent photoelectric coupling catalytic capability, requiring 309 mV overpotential to excite  $100 \text{ mA cm}^{-2}$  under illumination and maintaining stability for up to 48 h under different light conditions. Catalytic excellence stems from the elevated BIEF, which means Mn accelerated charge transport, modulated the charge density around the active center, effectively improving the catalytic activity. Moreover, the addition of Mn can effectively improve the conduction band (CB) and valence band (VB), reduce the energy band gap, improve the light absorption capacity and enhance the photocatalytic performance. This work provides new ideas for increasing the BIEF of heterojunction materials.

## 1. Introduction

In the process of clean energy transition, electrolysis of water to produce hydrogen has become one of the important ways to create green energy [1–5]. The hydrocracking reaction can be divided into two half-reactions, the two-electron hydrogen evolution reaction (HER) at the cathode and the four-electron oxygen evolution reaction (OER) at the anode, of which the OER is the decisive step in the overall reaction [6–10]. In order to overcome the severe limitations of the expensive and low earth content of the precious metals now used, non-precious metal-based materials, especially Fe, Co Ni-based compounds have been reported to be available for catalytic OER in alkaline environment [11–16]. The small tunability of the electronic configuration and active site of these catalysts limits their catalytic capacity. Therefore, the design of efficient OER catalyst compounds faces serious challenges.

Metal-organic frameworks (MOFs), as an organic-inorganic composite hybrid material, are considered ideal for electrocatalytic reactions due to tunable metal nodes and porous structure with a large specific surface area [17–20]. However, the photoelectrocatalytic ability of MOFs is limited by electronic configuration which has not been sufficiently exploited. The construction of heterojunctions is a viable option for modulating electrons, especially Mott Schottky heterojunctions

[21–25]. In addition, it has been shown that the catalytic activity can be effectively improved by modulating the BIEF of heterojunction [26–30]. For example, Fe-doped Ni phosphides/Ni sulfide p-p junction was synthesized by Zhang et al. using an iron doping strategy to improve BIEF, with good catalytic properties [31]. A bimetallic composite strategy was proposed by Nguyen et al. to prepare Ag-Zn-BTC/GO catalysts with improved photosensitivity of the material for efficient photodegradation reactions [32]. The above shows that metal doping is a very effective way to enhance the BIEF of a material. However, little research has been reported on the doping of MOFs compounds to enhance the BIEF of MOF-based Mott Schottky heterojunction materials to stimulate the potential catalytic activity of the materials.

Inspired by the above reflections, we have chosen Mn, a valence-variable element, for doping in Mott Schottky heterojunctions constructed by deposition of MOF semiconductor onto metal substrates using a more convenient, gentle and rapid electrosynthesis method [33, 34]. And to prevent metallic plating, the more reducible  $\text{KMnO}_4$  was added to the solution, which is also the source of the Mn element doping. Moreover, we selected FeBTC with good stability as the precursor [35]. The synthesized Mn-FeBTC/NiF has excellent electrocatalytic activity, requiring an overpotential of 338 mV to excite a current density of  $100 \text{ mA cm}^{-1}$ . And it is also very light-sensitive, requiring only 309 mV of

\* Corresponding authors.

E-mail addresses: [ymchai@upc.edu.cn](mailto:ymchai@upc.edu.cn) (Y.-M. Chai), [dongbin@upc.edu.cn](mailto:dongbin@upc.edu.cn) (B. Dong).

<https://doi.org/10.1016/j.apcatb.2023.122464>

Received 19 January 2023; Received in revised form 7 February 2023; Accepted 10 February 2023

Available online 11 February 2023

0926-3373/© 2023 Elsevier B.V. All rights reserved.

overpotential to drive a current density of  $100 \text{ mA cm}^{-1}$  under light. Exploration revealed that the modulation of the active site charge density by the enhancement of BIEF is the main reason for the increase in the catalytic capacity of Mn-FeBTC/NIF. Furthermore, Mn-FeBTC/NIF was found to exhibit stronger absorption in the visible wavelength range than undoped FeBTC/NIF. Mn-FeBTC/NIF can maintain a stable catalytic process over a long period of time under different light conditions, and in practice is not afraid of the effect of light changes on the intrinsic activity of the material, indicating its potential for large-scale use.

## 2. Experimental

### 2.1. Preparation of Mn-FeBTC/NIF

Firstly, solution A was prepared with 0.875 g of resorcinic acid and 15 ml of ethanol. And 3.01 g ferric nitrate tetrahydrate 0.05 g potassium permanganate and 35 ml deionized water were put into a beaker and stirred to obtain homogeneous solution B. And then, Solution A and solution B are mixed evenly to obtain the electrolyte to be used. Electrodeposition was carried out in a three-electrode system with a clean nickel-iron mesh as the working electrode, calomel electrode as the reference electrode and platinum plate as the counter electrode. In the experiment, the electricity was energized at a constant voltage of  $-2 \text{ V}$  for 1200 s, and then the product was cleaned with deionized water and ethanol and vacuum dried to obtain Mn-FeBTC/NIF.

### 2.2. Preparation of $\text{H}_2\text{O}_2$ -FeBTC/NIF

The experiment was the same as 2.1, except that  $\text{KMnO}_4$  was replaced with 1 ml  $\text{H}_2\text{O}_2$ . After cleaning and vacuum drying, the expected product  $\text{H}_2\text{O}_2$ -FeBTC/NIF was obtained.

### 2.3. Preparation of FeBTC/NIF

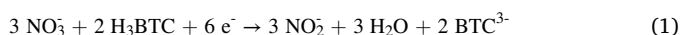
The experimental procedure was consistent with that in 2.1, but  $\text{KMnO}_4$  was not added when solution B was configured, and simple FeBTC/NIF was prepared.

### 2.4. Preparation of Mn(II)-FeBTC/NIF

The preparation process is the same as in 2.1, except that  $\text{KMnO}_4$  was replaced by manganese nitrate ( $\text{Mn}(\text{NO}_3)_2$ ). Mn(II)-FeCoBTC/NIF was prepared as the comparison sample.

## 3. Results and discussion

The synthesis process of the catalyst is shown in Fig. 1a. One-step electrodeposition on clean NIF at a constant voltage finally led to the Mn-FeBTC/NIF with a homogeneous sheet structure shown in Fig. 1a. Moreover, the reactions occurring on the NIF surface when a constant voltage is applied in the three-electrode system are illustrated in Fig. 1b. It has been reported in the literature that when this MOF structure is electrodeposited, the addition of an oxidizing agent to the electrolyte results in a competitive reaction with nitrate, thus altering the original reaction process [33]. Therefore,  $\text{KMnO}_4$  is chosen as a strong oxidant, so as to achieve not only the purpose of changing the reaction process, but also the goal of achieving Mn element doping. When  $\text{KMnO}_4$  is not added, reactions occurred in the experiment are as follows [33]:



As shown in Fig. 1b when  $\text{KMnO}_4$  is added to the electrolyte, it is  $\text{MnO}_4^-$  that will be the first to get electrons after energization, not the metal ions or  $\text{NO}_3^-$ , and the reaction as in Eq. 1 occurs. The reaction will produce 2–4 valent Mn ions and  $\text{BTC}^{3-}$ , both of which combine with iron

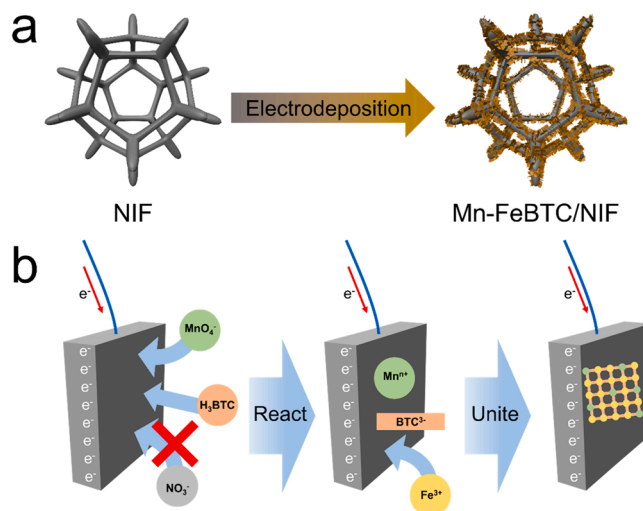
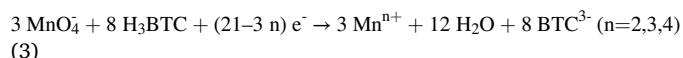


Fig. 1. (a) Schematic diagram of the Mn-FeBTC/NIF synthesis process; (b) Schematic representation of the competitive reactions that occur on the substrate surface during electrosynthesis.

ions to form a reticulated MOF structure (as Eq. 2).



A series of physical characterisations were used to characterise the prepared products and explore exactly what was synthesized. The material was first tested by XRD, and Fig. S1 showed that there is no characteristic peak position of FeBTC, indicating that the synthesized product is in an amorphous state. Then further IR tests were performed, and both pure BTC and synthetic FeBTC/NIF were also characterized comparatively (Fig. 2a). It can be seen that the sign peak of benzene ring at about  $3000 \text{ cm}^{-1}$  is shifted and weakened due to coordination with metal [36–38], which indicates the successful synthesis of MOF structure. A slight red shift of the peaks at  $715 \text{ cm}^{-1}$  and  $690 \text{ cm}^{-1}$  can be seen in the magnified view of the IR, which is also due to alignment.

In addition, the peak of the O-H bond of BTC at  $935 \text{ cm}^{-1}$  disappears in FeBTC, but reappears and is shifted in Mn-FeBTC. The disappearance and reappearance of the above findings is attributed to the difference in coordination numbers between Mn and Fe, with the doping of Mn causing a change in the conjugate structure resulting in uncoordinated carboxylates. Moreover, due to the low content of Mn, there are few uncoordinated carboxylic acids and the peak is small. In addition, peaks representing C-H at  $1004 \text{ cm}^{-1}$  and  $1605 \text{ cm}^{-1}$ , a peak representing C-O at  $1301 \text{ cm}^{-1}$  and an O-C=O peak position at  $1444 \text{ cm}^{-1}$  were found in the Raman test results for BTC, FeBTC/NIF and Mn-FeBTC/NIF (Fig. 2c) [39–41]. However, there is an offset at some peaks due to the coordination of the BTC to the metal. The above description demonstrates the successful synthesis of Mott Schottky heterojunctions FeBTC/NIF and Mn-FeBTC/NIF. To obtain the valence information of individual elements on the catalyst surface, XPS tests were performed on all samples. The survey of each sample show in Fig. S3. The XPS spectra of the different elements are presented in Fig. 2. The Mn 2p image (Fig. 2d) shows that the Mn element in the material has three valence states, 2+, 3+ and 4+ [42,43]. For Mn-FeBTC/NIF, the different oxidation states arise because of the different degrees of  $\text{KMnO}_4$  reduction. For Mn(II)-FeBTC/NIF, the different Mn oxidation states produced by the redox reaction of  $\text{Mn}^{2+}$  and  $\text{NO}_2^-$  in the electrolyte generated during electrodeposition. For element C (Fig. 2e), it can be seen that the peak at  $284.5 \text{ eV}$ , representing the C-C bond, and the peak at  $285.2 \text{ eV}$ , representing the C-O bond, are unchanged for each sample. However, the peak at  $288.9 \text{ eV}$  representing O=C-O is different for each comparison

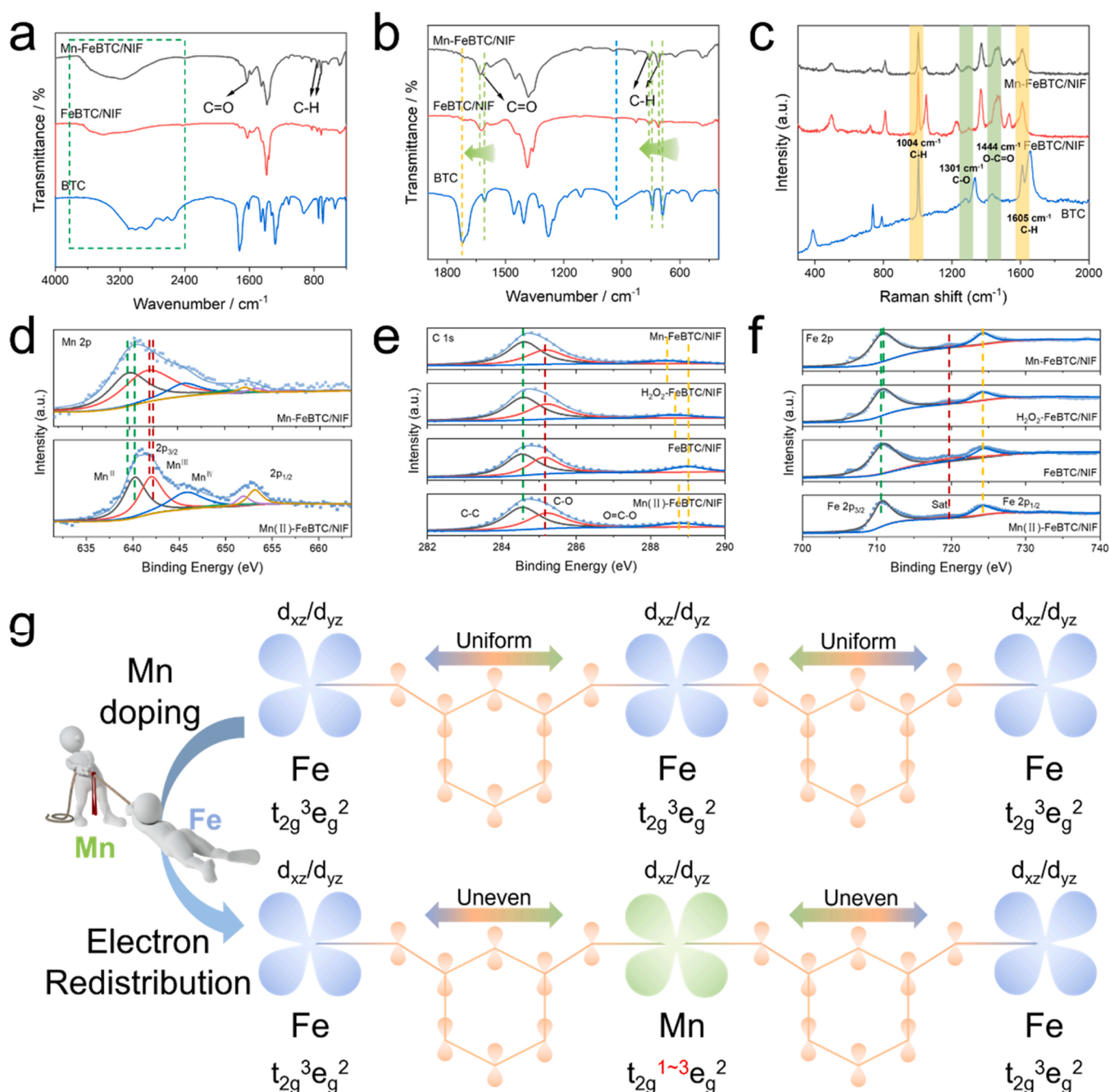


**Fig. 2.** (a) FTIR image of Mn-FeBTC/NIF, FeBTC/NIF and BTC; (b) Fig. b is the enlarged view of the area comparison of Fig. a; (c) Raman spectra of Mn-FeBTC/NIF, FeBTC/NIF and BTC; Fig. c is the enlarged view of the area comparison of Fig. b. XPS spectra of (d) Mn 2p; (e) C 1s; (f) Fe 2p; (g) Schematic comparison of the different assignments of electrons in the d-π conjugated system before and after Mn doping.

sample, which is due to the variation in alignment [44]. Fig. 2f shows the valence spectrum of Fe. The binding energy peaks at 710.6 eV and 724.2 eV belong to Fe 2p<sub>3/2</sub> and Fe 2p<sub>1/2</sub> of Fe<sup>3+</sup>. And the peak at Fe 2p<sub>3/2</sub> in Mn-FeBTC/NIF undergoes a slight positive shift relative to FeBTC/NIF, indicating a slight elevation of its valence state [18]. The mechanism for the change in the oxidation state of Fe is shown in Fig. 2g. For the BTC feedstock itself, the π-bonds on the benzene ring and the carboxylic acid form a large π-conjugated system. In the steric network structure of FeBTC, the carboxylate is coordinated to Fe. When it is coordinated with Fe to form a MOF, the π electrons form a d-π conjugate structure with the electrons in the d orbitals of Fe. When conjugation is created, the electrons in the organic ligands throughout the MOF are shared with the metal nodes and the system can reach a more stable state

through spontaneous electron adjustment. Under this strong conjugation effect, transition metal electrons can enhance the d<sub>xy</sub>/d<sub>yz</sub> orbital of the metal node Fe [45,46]. The electrons of the BTC are evenly dispersed towards the connected Fe metal. However, Mn is doped in with three different valence states, so three different scenarios 3, 4 and 5 electrons can exist in its d orbitals. This indicates that the d orbitals of Mn are not all in a stable half-full state, however the oxidation states of Fe are all 3 suggesting that the d orbitals are all in a stable semi-full case. At this moment Mn has a strong tendency to change to a half full state. Once the two are connected together in the same BTC, the d-π conjugation formed on both sides is not the same and the conjugated electrons are shifted towards the Mn ion which is in a non-half-full instability. This electron excursion is driven by a change in the system's natural tendency towards



a steady state. This redistribution of electrons occurs as Mn attracts the electrons around Fe towards itself through the d- $\pi$  conjugate structure. And although the Mn content is extremely small, it can radiate this influence throughout the material by means of this strong conjugation effect. Also because of the low Mn content, the increase in the valence of the Fe element after Mn doping is very slight.

To explore the morphology of the catalyst surface, SEM tests were performed on the samples (Fig. 3). From Fig. 3a-b, it can be seen that the microscopic surface of Mn-FeBTC/NIF has a uniform sheet-like nanostructure. The surface lamellar structure of the corresponding  $\text{H}_2\text{O}_2$ -FeBTC/NIF (Fig. 3c-d) is not very obvious, while the surface of FeBTC/NIF (Fig. 3e-f) and Mn(II)-FeBTC/NIF (Fig. 3g-h) do not even have lamellar morphology. This will cause their surface area to be smaller and carry fewer active sites, affecting the catalytic activity. To explore the element distribution on the surface of Mn-FeBTC/NIF, a mapping test (Fig. 3i) was conducted and found that Mn, Fe, C, O elements were uniformly distributed on the surface of the material. The EDS (Fig. S2) shows that Mn is doped into the catalyst at a very small amount.

A series of electrochemical characterizations were carried out to explore the OER catalytic properties of the material. The polarization curves of each comparison sample (Fig. 4a) were first tested in 1 M KOH solution under different light conditions. The different light situations

are 1) Dark. The beaker containing the electrolyte was wrapped in tinfoil to create light-free conditions on the catalyst surface; 2) Indoor Light. Tests were carried out during daylight hours without any applied treatment to the beaker; 3) Light. A xenon lamp apparatus is placed next to the three-electrode system used for testing, and artificial light is added perpendicular to the catalyst surface during the measurement. The data of Mn-FeBTC/NIF (Fig. S4),  $\text{H}_2\text{O}_2$ -FeBTC/NIF (Fig. S5); FeBTC/NIF (Fig. S6); Mn(II)-FeBTC/NIF (Fig. S7) are grouped together in Fig. 4a. The polarization curves of various samples in Fig. 4a are organized in Fig. 4b, so that the effect of changing light conditions on the catalytic performance of different samples can be more intuitively seen. And Fig. 4b shows that the overpotential decreases at a current density of  $100 \text{ mA cm}^{-2}$  with the gradual increase in light intensity from Dark to Indoor Light to Light. The values of the reduced potential for the individual catalyst samples are presented in Fig. 4b. The red line is the amount of reduced overpotential after the change from Dark to Indoor Light conditions, which can be seen to be similar. However, when the light intensity changed from Indoor Light to Light, a gap in the reduction of voltage appeared. From the comparison of FeBTC/NIF (15 mV) and Mn-FeBTC/NIF (33 mV), it can be seen that the doping of Mn can effectively improve the catalytic performance of FeBTC materials after the application of light. While the 7 mV of  $\text{H}_2\text{O}_2$ -FeBTC/NIF indicates

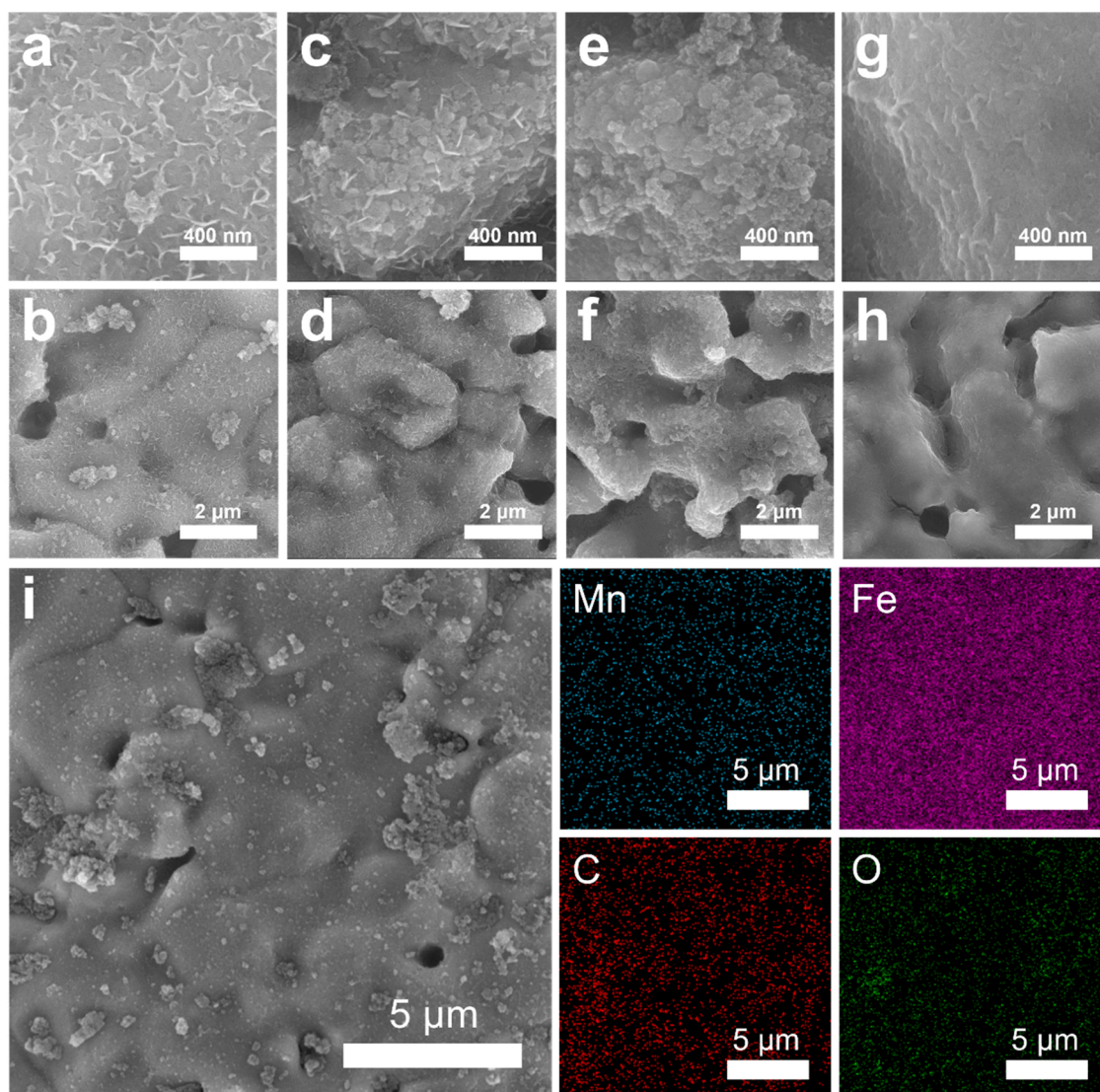


**Fig. 3.** Micromorphological characterization at different sizes (a) (d) Mn-FeBTC/NIF; (c) (d)  $\text{H}_2\text{O}_2$ -FeBTC/NIF; (e) (f) FeBTC/NIF; (g) (h) Mn(II)-FeBTC/NIF. (i) The mapping diagram of different elements on Mn-FeBTC/NIF.

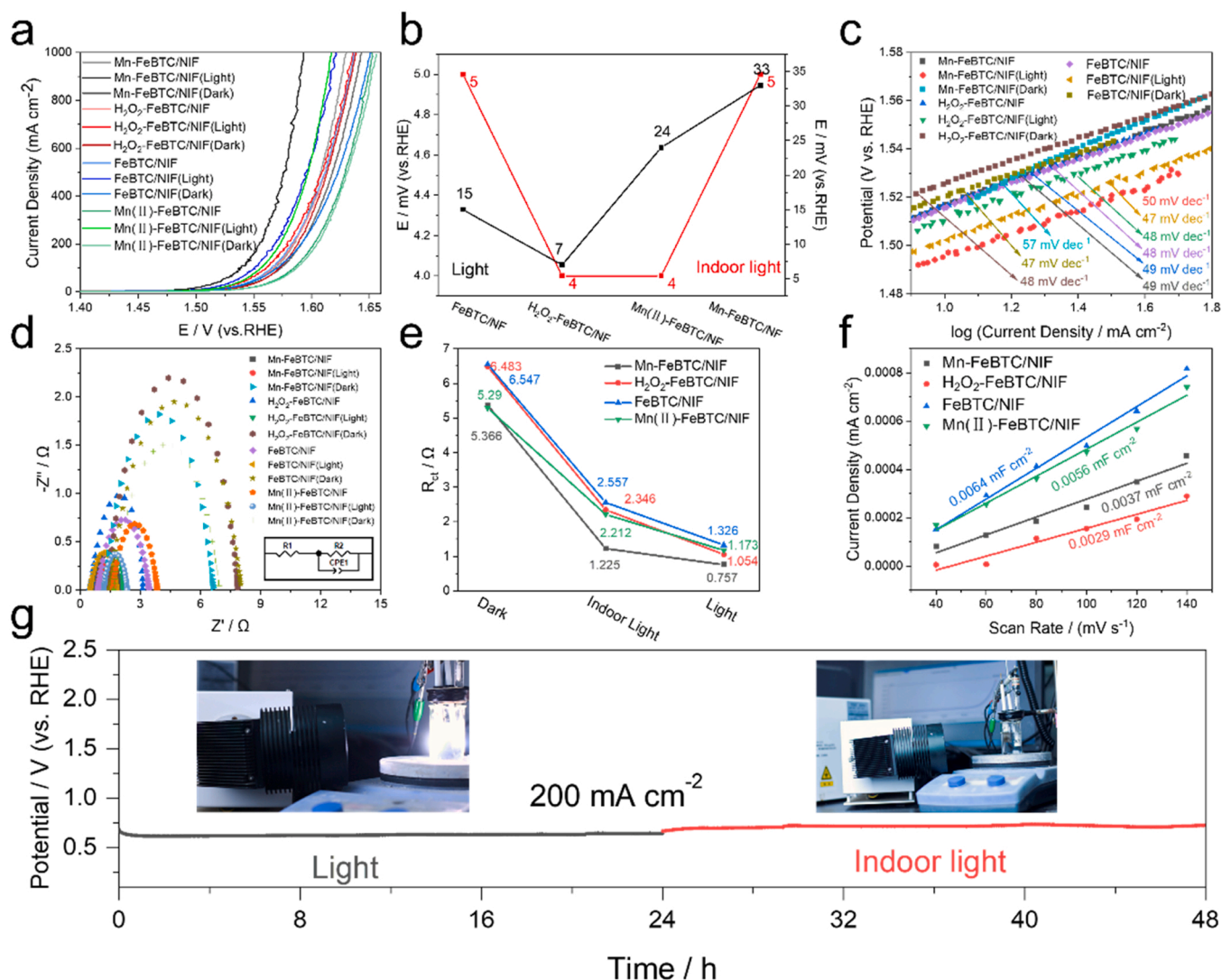


**Fig. 4.** (a) Polarization curves of each sample in 1 M KOH solution under different light conditions; (b) Line graph of the reduction in overpotential of each sample at 100 mA cm<sup>-2</sup> current density after a change in light intensity; (c) Tafel slope (d) EIS images (e) R<sub>ct</sub> (f) C<sub>dl</sub> of different samples under three types of light; (g) Mn-FeBTC/NiF constant current stability test at 200 mA cm<sup>-2</sup> for a long time under different light conditions. The black line shows the test under xenon light, the red line shows the test under indoor light conditions, and the pictures above show the test environment respectively.

that reduction of H<sub>2</sub>O<sub>2</sub> alone does not enhance or even diminish the sensitivity of the catalyst to light. Meanwhile, the Mn(II)-FeBTC/NiF prepared to demonstrate the importance of the reduction process was boosted by 24 mV. And as can be seen in Fig. S19, Mn(II)-FeBTC/NiF is actually a homogeneous junction consisting of MnBTC and FeBTC, which is described in more detail below. It is demonstrated that the addition of Mn elements can make the catalytic process of FeBTC more active under light, where the doping is more effective. To explore the reaction kinetics of the material, the Tafel slope of each sample (Fig. 4c) was analyzed and as can be seen from the graph, the gradient of all samples was around 48 mV dec<sup>-1</sup> under various light conditions, indicating that the addition of Mn did not change the reaction kinetic activity of the catalyst itself. Impedance is also an important measure of catalyst performance and the products have been characterized accordingly. By combining the different catalyst data (Fig. S8-11) in Fig. 4d, it is clear that there are three kinds of half circles with different curvatures depending on the lighting conditions. The circuit diagram used for the fit is shown in the box inserted in Fig. 4d. In order to see the trend more clearly, the impedance data for each substance under different light treatments was plotted as a line graph (Fig. 4e). Fig. 4e shows that as the horizontal coordinate changes from left to right

conditions, the vertical coordinate of each sample then becomes smaller. As the light intensity of the material surface gradually increases, the resistance decreases significantly. The conductivity of FeBTC/NiF without special treatment is the worst under all conditions, indicating that the original structure is not conducive to carrier transport. Moreover, the resistance of Mn-FeBTC/NiF was found to be no higher than that of the other comparison samples under different illuminations, indicating that the modulation of d-π conjugation by the addition of Mn element can effectively increase the conductivity of FeBTC. In addition, the respective C<sub>dl</sub> (Fig. 4f) was also measured from the CV data (Fig. S12-15) of each sample, which is exactly proportional to the electrochemical active surface area (ECSA). The comparative data show that C<sub>dl</sub> becomes smaller with the addition of H<sub>2</sub>O<sub>2</sub>, while the presence of Mn in the catalyst increases C<sub>dl</sub>, suggesting that Mn can effectively modulate the micromorphology during electrodeposition to improve ECSA. Stability is considered to be one of the most important measures of catalyst quality, so Mn-FeBTC/NiF (Fig. 4g) was tested for stability over a long period of time under different light conditions. The test was carried out in two stages, firstly in a Light environment for 24 h as shown in the photo on the black line in Fig. 4g. In the second stage, the xenon lamp was switched off and the test continued for 24 h using the samples from the

first session. The photo above the red line in Fig. 4g shows the test environment. The samples were also morphologically characterized after the measurements and the lamellar structure was found to be agglomerated into balls but uniformly dispersed (Fig. S16). The XRD characterization of this material shows that the test has little effect on its structure (Fig. S17). Valence analysis reveals that only Fe is elevated in the surface elements and nothing else is changed (Fig. S18). These demonstrate the good catalytic stability of Mn-FeBTC under various light conditions.

Estimation of valence band (VB) and conduction band (CB) positions is a common method for assessing the potential of semiconductor catalysts in the redox process of water. Therefore, the analysis of the XPS of the sample to determine VB energy [47,48]. The VB marked in Fig. 5a are Mn-FeBTC/NIF (−0.39 eV), H<sub>2</sub>O<sub>2</sub>-FeBTC/NIF (−1.3 eV), FeBTC/NIF (−1.52 eV), Mn(II)-FeBTC/NIF (−0.62 eV). Comparison reveals that Mn doping is one of the effective ways to increase VB energy. To determine the position of the CB, the magnitude of the band gap energy (Fig. 5b) is

calculated by equation  $(\alpha h\nu)^2 \propto h\nu - E_g$ , where  $\alpha$ ,  $h$ ,  $\nu$  and  $E_g$  are the absorption coefficient, Planck's constant, optical frequency and band gap energy respectively [49,50]. In addition, the absorption intensity of Mn-FeBTC/NIF and FeBTC/NIF for different wavelengths of ultraviolet light from 200 nm to 800 nm was also tested for comparison (Fig. 5c). Mn-FeBTC/NIF was found to absorb more light from 380 nm to 800 nm, reaching a maximum percentage increase of 68.5% at 738 nm (Fig. S19) and a 0.28 increase in maximum absorption intensity at 597 nm (Fig. S20), owing to the increased photosensitivity due to the reduced energy band gap.

Schematic diagram (Fig. 5d) of the energy band distribution before and after Mn doping into FeBTC from the data obtained. According to Fig. 5d, both CB and VB of Mn-FeBTC/NIF have increased relative to FeBTC/NIF, by 0.99 eV, 1.13 eV respectively. Both are simultaneously enhanced to demonstrate that when Mn was used instead of Fe, resulting in higher mobility and better photogenerated carrier consumption in the original MOF. Moreover, the growth of the CB minimum can also

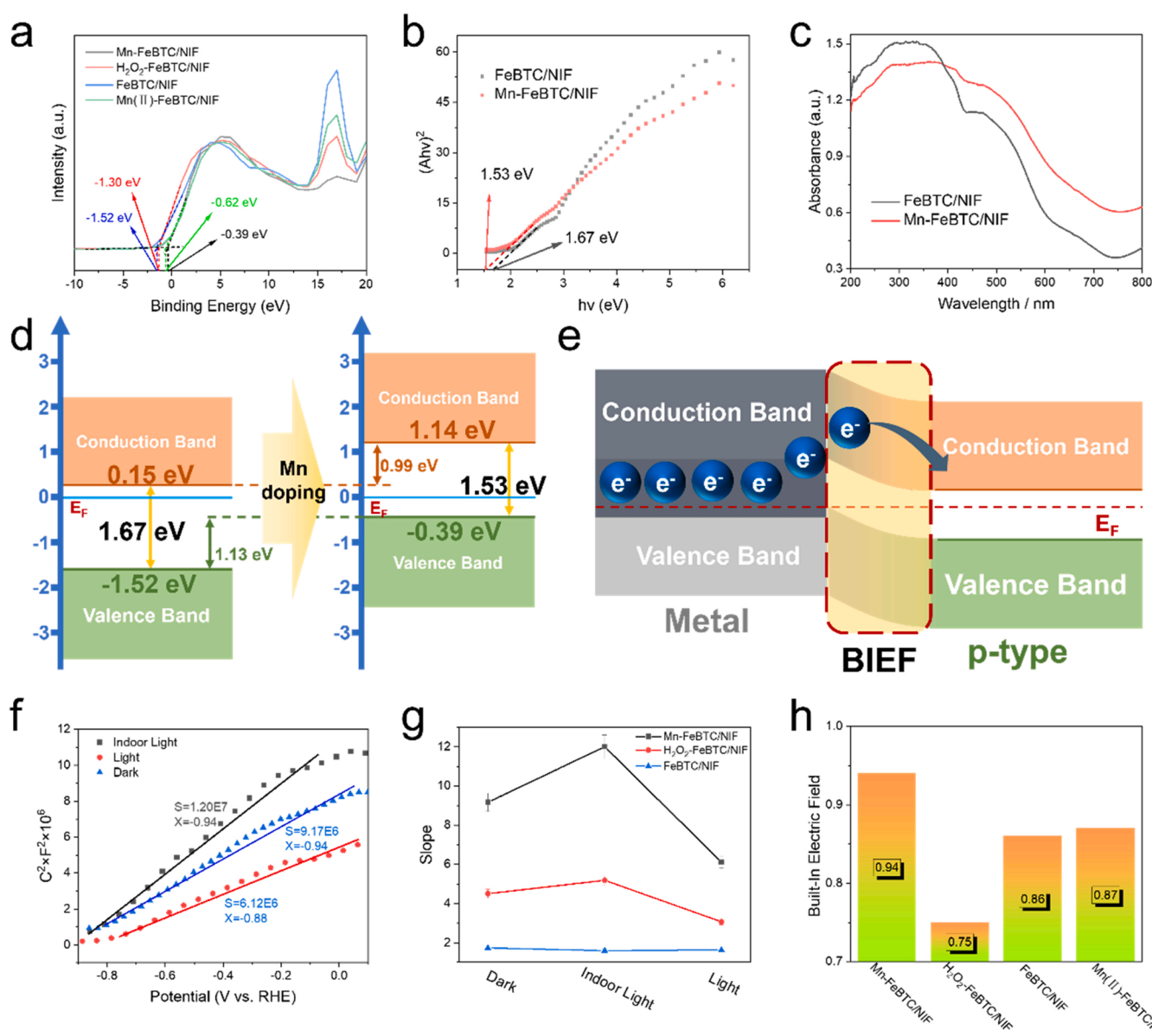


**Fig. 5.** (a) Valence band plot for each sample fitted by XPS spectrogram; (b) Band gap estimated from the correlation curve of  $(\alpha h\nu)^{1/2}$  with photon energy; (c) UV/Vis absorption spectra of Mn-FeBTC/NIF and FeBTC/NIF; (d) Schematic diagram of the energy band structure of Mn-FeBTC/NIF and FeBTC/NIF; (e) Schematic diagram of the Mott Schottky heterojunction interface; (f) MS plots of Mn-FeBTC/NIF under various light; (g) Slope and (h) BIEF of each sample fitted by MS plots in different environments.



effectively increase the activity of photogenerated carrier interactive reaction on the material interface [47]. Another key point is the reduction in the forbidden band width, where the addition of Mn reduces the band gap of the FeBTC from 1.67 eV to 1.53 eV. Many elements are reported in the literature to be doped for the purpose of energy level modulation, such as Zn [51], Ag [52], Co [53] and so on. The jump of photogenerated carriers from the valence band to the conduction band, matched to the photoelectric effect model. And for the photoelectric effect, described by equation  $E_k = h\nu - W$ , where  $E_k$  is electron kinetic energy,  $h$  is Planck's constant,  $\nu$  is frequency of incident light,  $W$  is electron escape function. For the valence band, the minimum escape work to be overcome by the photogenerated carriers is equal to the energy band gap size. When  $E_k$  is equal to 0, this is the minimum frequency at which light can excite carriers, according to the formula and the existing energy band gap value, it can be concluded that the minimum frequency requirement for light extends from  $4.03 \times 10^{14} \text{ s}^{-1}$  to  $3.69 \times 10^{14} \text{ s}^{-1}$ , which means that the same beam of light can produce more photogenerated carriers. Based on the relationship between the wavelength and frequency of light, the upper wavelength of light that can excite carriers is extended from 744 nm to 813 nm. As reflected in the data, the doping of Mn effectively extends the light acceptance range of FeBTC.

When Mn-FeBTC comes into contact with a metal substrate, a mobile rearrangement of electrons and holes occurs, and a built-in potential is formed at the contact interface as shown in Fig. 5e. The BIEF is generated mainly from the redistribution of carriers at the contact interface between the semiconductor and the conducting substrate, and the size of the distribution is the size of the BIEF. Further studies were carried out to test the Mott Schottky (MS) curve on samples under different light. The formula for the MS curve is listed below [54]:

$$\frac{1}{C^2} = \frac{2}{\epsilon \epsilon_0 e N_D} (E - E_{fb} - \frac{k_B T}{e}) \quad (5)$$

In the formula,  $C$  is the space charge capacitance,  $\epsilon$  and  $\epsilon_0$  represent the dielectric constant of the semiconductor and the dielectric constant in vacuum,  $e$  is the electron charge, and  $N_D$  is the carrier density. Further derivation of the carrier density  $N_D$  can be obtained by the following formula:

$$N_D = \frac{2}{\epsilon \epsilon_0 e} \frac{dE}{d\frac{1}{C^2}} = \frac{2}{\epsilon \epsilon_0 e} \frac{1}{\text{slope}} \quad (6)$$

where the slope is the slope of the data fit in the MS curve. As can be seen from the graph, the slopes are all positive, proving that both are n-type semiconductors [55–57]. The Mott Schottky heterojunction is formed when the semiconductor is in direct contact with the conductor. The FeBTC synthesized on the metallic NIF substrate was found to be an n-type semiconductor in the MS curve, and this structure is exactly the configuration of the Mott Schottky heterojunction. The MS plots of Mn-FeBTC/NIF (Fig. 5f) show that the slope increases first and then decreases with increasing light intensity, proving that the carrier density is a decreasing and then increasing phenomenon [58]. Converging the data for slopes in  $\text{H}_2\text{O}_2$ -FeBTC/NIF (Fig. S21), FeBTC/NIF (Fig. S22) in a single graph (Fig. 5g), the same situation is found to exist. This is due to the fact that the current-carrying substrates created by the low light environment have an effect on the original carriers of the material, while this effect is not present in strong light. In addition, two segments with different slopes can be seen in Mn(II)-FeBTC/NIF (Fig. S23). This is due to the fact that the divalent manganese ions added during electrodeposition form a homogeneous junction between MnBTC and FeBTC, rather than a doped structure, which is less effective for the modulation of FeBTC compared to doping. It was found that Mn-FeBTC/NIF had the largest BIEF after comparing the different structures (Fig. 5h). And it can be seen from Fig. 5h that the slope of Mn-FeBTC/NIF is larger than that of FeBTC/NIF, indicating that the doping of Mn adjusts the carrier distribution and density in FeBTC. This regulation mainly comes from the

large effect of Mn doping on the original d- $\pi$  conjugation described in the previous section, which changes the original electron distribution, and the carrier distribution and density change with it. This change expands the carrier redistribution at the interface of FeBTC and NIF, which increases the BIEF. And this increase in BIEF caused by Mn doping indicates that this method has a greater effect on the charge density around active center, which can effectively increase the activity [26–28, 34].

#### 4. Conclusions

In this work, Mn-FeBTC/NIF was synthesized by adding a strong oxidizing agent,  $\text{KMnO}_4$ , to the electrolyte for the purpose of doping as well as avoiding metal plating. The BIEF of the Mott Schottky heterojunction formed by the FeBTC of the n-type semiconductor and metal substrate is effectively modulated by Mn doping. Elevated BIEF modulates the charge density near the active site of Mn-FeBTC/NIF, effectively increasing the catalytic activity. Besides, Mn-FeBTC/NIF has higher valence and conduction bands and a smaller energy band gap, resulting in better light absorption, which indicates its excellent photoelectrocatalysis capability. And it can maintain for 48 h at a current density of  $200 \text{ mA cm}^{-2}$  under different lighting conditions with almost no change in voltage, which proves its excellent stability. This study proposes that Mn doping can modulate the BIEF of MOF-based Mott Schottky heterojunction materials, which will promote the wide application of MOFs in photoelectrocatalysis.

#### CRediT authorship contribution statement

**Yi-Wen Dong:** Data curation, Writing - original draft, Formal analysis, Investigation, Writing - review & editing, **Hai-Jun Liu:** Writing - original draft, Conceptualization, Formal analysis, Writing - review & editing, **Xiao Wang:** Writing - review & editing, Formal analysis, **Fu-Li Wang:** Writing - original draft, Methodology, **Xin-Yu Zhang:** Writing - original draft, Formal analysis, **Qian-Xi Lv:** Writing - original draft, Writing - review & editing, **Chun-Ying Liu:** Writing - review & editing, Formal analysis, **Yong-Ming Chai:** Funding acquisition, Conceptualization, Investigation, Resources, Formal analysis, Supervision, Writing - review & editing, **Bin Dong:** Formal analysis, Investigation, Resources, Writing - original draft, Funding acquisition, Project administration, Writing - review & editing.

#### Declaration of Competing Interest

The authors declare that they have no known competing financial interests or personal relationships that could have appeared to influence the work reported in this paper.

#### Data availability

Data will be made available on request.

#### Acknowledgements

This work is financially supported by National Natural Science Foundation of China (52174283 and 52274308).

#### Appendix A. Supporting information

Supplementary data associated with this article can be found in the online version at doi:10.1016/j.apcatb.2023.122464.

#### References

- [1] Y. Sun, H. Liao, J. Wang, B. Chen, S. Sun, S.J.H. Ong, S. Xi, C. Diao, Y. Du, J. O. Wang, M.B.H. Breese, S. Li, H. Zhang, Z.J. Xu, Covalency competition dominates

- the water oxidation structure–activity relationship on spinel oxides, *Nat. Catal.* 2 (2020) 554–563.
- [2] J. Zhou, L. Yu, Q. Zhou, C. Huang, Y. Zhang, B. Yu, Y. Yu, Ultrafast fabrication of porous transition metal foams for efficient electrocatalytic water splitting, *Appl. Catal. B: Environ.* 288 (2021), 120002.
  - [3] X. Yu, C. Hu, P. Ji, Y. Ren, H. Zhao, G. Liu, R. Xu, X. Zhu, Z. Li, Y. Ma, L. Ma, Optically transparent ultrathin NiCo alloy oxide film: Precise oxygen vacancy modulation and control for enhanced electrocatalysis of water oxidation, *Appl. Catal. B: Environ.* 310 (2022), 121301.
  - [4] J. Zhou, Z. Han, X. Wang, H. Gai, Z. Chen, T. Guo, X. Hou, L. Xu, X. Hu, M. Huang, S.V. Levchenko, H. Jiang, Discovery of quantitative electronic structure-OER activity relationship in metal-organic framework electrocatalysts using an integrated theoretical-experimental approach, *Adv. Funct. Mater.* 31 (2021), 2102066.
  - [5] T. Wang, X. Cao, L. Jiao, Ni<sub>2</sub>P/NiMoP heterostructure as a bifunctional electrocatalyst for energy-saving hydrogen production, *eScience* 1 (2021) 69–74.
  - [6] Y.N. Zhou, W.L. Yu, Y.N. Cao, J. Zhao, B. Dong, Y. Ma, F.L. Wang, R.Y. Fan, Y. L. Zhou, Y.M. Chai, S-doped nickel-iron hydroxides synthesized by room-temperature electrochemical activation for efficient oxygen evolution, *Appl. Catal. B: Environ.* 292 (2021), 120150.
  - [7] H. Liao, X. Zhang, S. Niu, P. Tan, K. Chen, Y. Liu, G. Wang, M. Liu, J. Pan, Dynamic dissolution and re-adsorption of molybdate ion in iron incorporated nickel-molybdenum oxyhydroxide for promoting oxygen evolution reaction, *Appl. Catal. B: Environ.* 307 (2022), 121150.
  - [8] H. Chen, X. Liang, Y. Liu, X. Ai, T. Asefa, X. Zou, Active site engineering in porous electrocatalysts, *Adv. Mater.* 32 (2020), 2002435.
  - [9] J. Li, Oxygen evolution reaction in energy conversion and storage: design strategies under and beyond the energy scaling relationship, *Nano-Micro Lett.* 14 (2022) 112.
  - [10] R. Yang, X. Shi, Y. Wang, J. Jin, H. Liu, J. Yin, Y.Q. Zhao, P. Xi, Ruthenium-modified porous NiCo<sub>2</sub>O<sub>4</sub> nanosheets boost overall water splitting in alkaline solution, *Chin. Chem. Lett.* 33 (2022) 4930–4935.
  - [11] W. Wang, Z. Wang, Y. Hu, Y. Liu, S. Chen, A potential-driven switch of activity promotion mode for the oxygen evolution reaction at Co<sub>3</sub>O<sub>4</sub>/NiOxHy interface, *eScience* 2 (2022) 438–444.
  - [12] H. Yang, L. Gong, H. Wang, C. Dong, J. Wang, K. Qi, H. Liu, X. Guo, B.Y. Xia, Preparation of nickel-iron hydroxides by microorganism corrosion for efficient oxygen evolution, *Nat. Commun.* 11 (2020) 5075.
  - [13] J.Y. Zhang, Y. Yan, B. Mei, R. Qi, T. He, Z. Wang, W. Fang, S. Zaman, Y. Su, S. Ding, B.Y. Xia, Local spin-state tuning of cobalt–iron selenide nanoframes for the boosted oxygen evolution, *Energy Environ. Sci.* 14 (2021) 365–373.
  - [14] R.Y. Fan, J.Y. Xie, H.J. Liu, H.Y. Wang, M.X. Li, N. Yu, R.N. Luan, Y.M. Chai, B. Dong, Directional regulating dynamic equilibrium to continuously update electrocatalytic interface for oxygen evolution reaction, *Chem. Eng. J.* 431 (2022), 134040.
  - [15] Y. Wang, S. Chen, S. Zhao, Q. Chen, J. Zhang, Interfacial coordination assembly of tannic acid with metal ions on three-dimensional nickel hydroxide nanowalls for efficient water splitting, *J. Mater. Chem. A* 8 (2020) 15845–15852.
  - [16] Y. Wang, J. Ma, J. Wang, S. Chen, H. Wang, J. Zhang, Interfacial Scaffolding Preparation of Hierarchical PBA-based Derivative Electrocatalysts for Efficient Water Splitting, *Adv. Energy Mater.* 9 (2019), 1802939.
  - [17] A. Radwan, H. Jin, D. He, S. Mu, Design Engineering, Synthesis Protocols, and Energy Applications of MOF-Derived Electrocatalysts, *Nano-Micro Lett.* 13 (2021) 132.
  - [18] H. Jia, N. Yao, J. Zhu, Y. Liu, Y. Lao, H. Cong, W. Luo, Ni<sub>3</sub>N Modified MOF Heterostructure with Tailored Electronic Structure for Efficient Overall Water Splitting, *Chin. J. Struct. Chem.* 41 (2022) 2208031–2208036.
  - [19] Y. Wei, X. Zhang, Z. Wang, J. Yin, J. Huang, G. Zhao, X. Xu, Metal-organic framework derived NiCoP hollow polyhedrons electrocatalyst for pH-universal hydrogen evolution reaction, *Chin. Chem. Lett.* 32 (2021) 119–124.
  - [20] W.W. Li, T.Z. Tian, M. Yang, N.W. Li, L. Yu, Formation of hollow frameworks of dual-sided Fe/Fe<sub>3</sub>C@N-doped carbon nanotubes as bifunctional oxygen electrocatalyst for Zn-air batteries, *Appl. Catal. B: Environ.* 317 (2022), 121760.
  - [21] S.W. LaGasse, P. Dhakras, K. Watanabe, T. Taniguchi, J.U. Lee, Gate-Tunable Graphene–WSe<sub>2</sub> Heterojunctions at the Schottky–Mott Limit, *Adv. Mater.* 31 (2019), 1901392.
  - [22] M. Tan, C. Yu, Q. Luan, C. Liu, W. Dong, Y. Su, L. Qiao, L. Gao, Q. Lu, Y. Bai, The Mott–Schottky heterojunction MoC@NG@ZIS with enhanced kinetic response for promoting photocatalytic hydrogen production, *J. Mater. Chem. A* 10 (2022) 21465–21473.
  - [23] H. Yang, B. Wang, S. Kou, G. Lu, Z. Liu, Mott-Schottky heterojunction of Co/Co<sub>2</sub>P with built-in electric fields for bifunctional oxygen electrocatalysis and zinc-air battery, *Chem. Eng. J.* 425 (2021), 131589.
  - [24] L. Peng, L. Su, X. Yu, R. Wang, X. Cui, H. Tian, S. Cao, B.Y. Xia, J. Shi, Electron redistribution of ruthenium-tungsten oxides Mott-Schottky heterojunction for enhanced hydrogen evolution, *Appl. Catal. B: Environ.* 308 (2022), 121229.
  - [25] L. Deng, K. Zhang, D. Shi, S. Liu, D. Xu, Y. Shao, J. Shen, Y. Wu, X. Hao, Rational design of Schottky heterojunction with modulating surface electron density for high-performance overall water splitting, *Appl. Catal. B: Environ.* 299 (2021), 120660.
  - [26] Y. Kang, S. Wang, K.S. Hui, S. Wu, D.A. Dinh, X. Fan, F. Bin, F. Chen, J. Geng, W.-C. M. Cheong, K.N. Hui, Surface reconstruction establishing Mott-Schottky heterojunction and built-in space-charging effect accelerating oxygen evolution reaction, *Nano Res.* 15 (2022) 2952–2960.
  - [27] M. Yuan, J. Chen, Y. Bai, Z. Liu, J. Zhang, T. Zhao, Q. Wang, S. Li, H. He, G. Zhang, Unveiling Electrochemical Urea Synthesis by Co-Activation of CO<sub>2</sub> and N<sub>2</sub> with Mott–Schottky Heterostructure Catalysts, *Angew. Chem. Int. Ed.* 60 (2021) 10910–10918.
  - [28] T. Li, J. Yin, D. Sun, M. Zhang, H. Pang, L. Xu, Y. Zhang, J. Yang, Y. Tang, J. Xue, Manipulation of Mott–Schottky Ni/CeO<sub>2</sub> Heterojunctions into N-Doped Carbon Nanofibers for High-Efficiency Electrochemical Water Splitting, *Small* 18 (2022), 2106592.
  - [29] X. Wang, G. Zhan, Y. Wang, Y. Zhang, J. Zhou, R. Xu, H. Gai, H. Wang, H. Jiang, M. Huang, Engineering core-shell Co<sub>9</sub>S<sub>8</sub>/Co nanoparticles on reduced graphene oxide: Efficient bifunctional Mott–Schottky electrocatalysts in neutral rechargeable Zn–Air batteries, *J. Energy Chem.* 68 (2022) 113–123.
  - [30] S. Zhang, C. Zhang, X. Zheng, G. Su, H. Wang, M. Huang, Integrating electrophilic and nucleophilic dual sites on heterogeneous bimetallic phosphide via enhancing interfacial electronic field to boost hydrazine oxidation and hydrogen evolution, *Appl. Catal. B: Environ.* 324 (2023), 122207.
  - [31] J. Zhang, H. Yu, J. Yang, X. Zhu, M. Hu, J. Yang, Heterostructure engineering of the Fe-doped Ni phosphides/Ni sulfide p-p junction for high-efficiency oxygen evolution, *J. Alloy. Compd.* 924 (2022), 166613.
  - [32] M.B. Nguyen, G.H. Le, T.D. Nguyen, K.K. Nguyen, T.T.T. Pham, T. Lee, T.A. Vu, Bimetallic Ag-Zn-BTC/GO composite as highly efficient photocatalyst in the photocatalytic degradation of reactive yellow 145 dye in water, *J. Hazard. Mater.* 420 (2021), 126560.
  - [33] S. Xie, W. Monnens, K. Wan, W. Zhang, W. Guo, M. Xu, I.F.J. Vankelecom, X. Zhang, J. Franssaer, Cathodic Electrodeposition of MOF Films Using Hydrogen Peroxide, *Angew. Chem. Int. Ed.* 60 (2021) 24950–24957.
  - [34] X. Zhao, M. Liu, Y. Wang, Y. Xiong, P. Yang, J. Qin, X. Xiong, Y. Lei, Designing a Built-In Electric Field for Efficient Energy Electrocatalysis, *ACS Nano* 16 (2022) 19959–19979.
  - [35] Y. Wang, L. Zhao, J. Ma, J. Zhang, Confined interface transformation of metal–organic frameworks for highly efficient oxygen evolution reactions, *Energy Environ. Sci.* 15 (2022) 3830–3841.
  - [36] N. Torres, J. Galicia, Y. Plasencia, A. Cano, F. Echevarria, L.F. Desdin-Garcia, E. Reguera, Implications of structural differences between Cu-BTC and Fe-BTC on their hydrogen storage capacity, *Colloids Surf. A: Physicochem. Eng. Asp.* 549 (2018) 138–146.
  - [37] Y. Yang, Y. Bai, F. Zhao, E. Yao, J. Yi, C. Xuan, S. Chen, Effects of metal organic framework Fe-BTC on the thermal decomposition of ammonium perchlorate, *RSC Adv.* 6 (2016) 67308–67314.
  - [38] D. Tocco, C. Carucci, D. Todde, K. Shortall, F. Otero, E. Sanjust, E. Magner, A. Salis, Enzyme immobilization on metal organic frameworks: Laccase from *Aspergillus* sp. is better adapted to ZIF-zni rather than Fe-BTC, *Colloids Surf. B: Biointerfaces* 208 (2021), 112147.
  - [39] D. Chen, Q. Sun, C. Han, Y. Guo, Q. Huang, W.A. Goddard, J. Qian, Enhanced oxygen evolution catalyzed by in situ formed Fe-doped Ni oxyhydroxides in carbon nanotubes, *J. Mater. Chem. A* 10 (2022) 16007–16015.
  - [40] D. Chen, Q. Sun, C. Han, Y. Guo, Q. Huang, W.A. Goddard, J. Qian, Enhanced oxygen evolution catalyzed by in situ formed Fe-doped Ni oxyhydroxides in carbon nanotubes, *J. Mater. Chem. A* 10 (2022) 16007–16015.
  - [41] I. Strauss, A. Mundstock, D. Hinrichs, R. Himstedt, A. Knebel, C. Reinhardt, D. Dorfs, J. Caro, The Interaction of Guest Molecules with Co-MOF-74: A Vis/NIR and Raman Approach, *Angew. Chem. Int. Ed.* 57 (2018) 7434–7439.
  - [42] M. Kaur, M. Chhetri, C.N.R. Rao, Photoelectrochemical OER activity by employing BiVO<sub>4</sub> with manganese oxide co-catalysts, *Phys. Chem. Chem. Phys.* 22 (2020) 811–817.
  - [43] M. Sun, R.-T. Gao, X. Liu, R. Gao, L. Wang, Manganese-based oxygen evolution catalysts boosting stable solar-driven water splitting: MnSe as an intermetallic phase, *J. Mater. Chem. A* 8 (2020) 25298–25305.
  - [44] P. Goyal, A. Paruthi, D. Menon, R. Behara, A. Jaiswal, K. V. A. Kumar, V. Krishnan, S.K. Misra, Fe doped bimetallic HKUST-1 MOF with enhanced water stability for trapping Pb(II) with high adsorption capacity, *Chem. Eng. J.* 430 (2022), 133088.
  - [45] Y. Ni, L. Lin, Y. Shang, L. Luo, L. Wang, Y. Lu, Y. Li, Z. Yan, K. Zhang, F. Cheng, J. Chen, Regulating Electrocatalytic Oxygen Reduction Activity of a Metal Coordination Polymer via d– $\pi$  Conjugation, *Angew. Chem. Int. Ed.* 60 (2021) 16937–16941.
  - [46] X. Cao, L. Zhao, B. Wulan, D. Tan, Q. Chen, J. Ma, J. Zhang, Atomic Bridging Structure of Nickel–Nitrogen–Carbon for Highly Efficient Electrocatalytic Reduction of CO<sub>2</sub>, *Angew. Chem. Int. Ed.* 61 (2022), e202113918.
  - [47] W. Yang, L. Zhang, J. Xie, X. Zhang, Q. Liu, T. Yao, S. Wei, Q. Zhang, Y. Xie, Enhanced Photoexcited Carrier Separation in Oxygen-Doped ZnIn<sub>2</sub>S<sub>4</sub> Nanosheets for Hydrogen Evolution, *Angew. Chem. Int. Ed.* 55 (2016) 6716–6720.
  - [48] Z. Liang, X. Bai, P. Hao, Y. Guo, Y. Xue, J. Tian, H. Cui, Full solar spectrum photocatalytic oxygen evolution by carbon-coated TiO<sub>2</sub> hierarchical nanotubes, *Appl. Catal. B: Environ.* 243 (2019) 711–720.
  - [49] Y. Zhu, Q. Liang, M. Zhou, C. Yao, S. Xu, Z. Li, Triptycene-Based Polymer Embedded in ZnIn<sub>2</sub>S<sub>4</sub> to Construct a Hierarchical Heterostructure for Efficient Photocatalytic Hydrogen Evolution, *ACS Applied Energy Materials* 4 (2021) 13239–13247.
  - [50] S. Wang, B.Y. Guan, X. Wang, X.W.D. Lou, Formation of Hierarchical Co<sub>9</sub>S<sub>8</sub>@ZnIn<sub>2</sub>S<sub>4</sub> Heterostructured Cages as an Efficient Photocatalyst for Hydrogen Evolution, *J. Am. Chem. Soc.* 140 (2018) 15145–15148.
  - [51] Y. Shi, Y. Zhou, D.-R. Yang, W.-X. Xu, C. Wang, F.-B. Wang, J.-J. Xu, X.-H. Xia, H.-Y. Chen, Energy Level Engineering of MoS<sub>2</sub> by Transition-Metal Doping for Accelerating Hydrogen Evolution Reaction, *J. Am. Chem. Soc.* 139 (2017) 15479–15485.
  - [52] W. Xu, H. Yang, C. Liu, Z. Zhang, C. Chen, Z. Ye, Z. Lu, X. Wang, J. Gao, J. Chen, Z. Xie, L. Miao, Optimized Electronic Bands and Ultralow Lattice Thermal



- Conductivity in Ag and Y Codoped SnTe, *ACS Appl. Mater. Interfaces* 13 (2021) 32876–32885.
- [53] H. Zhao, X. Xu, C. Li, R. Tian, R. Zhang, R. Huang, Y. Lyu, D. Li, X. Hu, L. Pan, Y. Wang, Cobalt-doping in Cu<sub>2</sub>SnS<sub>3</sub>: enhanced thermoelectric performance by synergy of phase transition and band structure modification, *J. Mater. Chem. A* 5 (2017) 23267–23275.
- [54] B.K. Kim, M.J. Kim, J.J. Kim, Modulating the active sites of nickel phosphorous by pulse-reverse electrodeposition for improving electrochemical water splitting, *Appl. Catal. B: Environ.* 308 (2022), 121226.
- [55] G. Heidari, M. Rabani, B. Ramezanzadeh, Application of CuS–ZnS PN junction for photoelectrochemical water splitting, *Int. J. Hydrog. Energy* 42 (2017) 9545–9552.
- [56] F.A. Chaves, P.C. Feijoo, D. Jiménez, 2D pn junctions driven out-of-equilibrium, *Nanoscale Adv.* 2 (2020) 3252–3262.
- [57] S. Hamrouni, M.S. AlKhalifah, M.S. El-Bana, S.K. Zobaidi, S. Belgacem, Deposition and characterization of spin-coated n-type ZnO thin film for potential window layer of solar cell, *Appl. Phys. A* 124 (2018) 555.
- [58] C. Masante, M. Kah, C. Hébert, N. Rouger, J. Pernot, Non-Volatile Photo-Switch Using a Diamond pn Junction, *Adv. Electron. Mater.* 8 (2022), 2100542.